Journal of
Materials Chemistry A

This article can be cited before page numbers have been issued, to do this please use: J. Xu, H. Zhou, K. Shi, R. Yan, Y. Tang, J. Liu, J. Ye, D. Zhang and T. Fan, *J. Mater. Chem. A*, 2016, DOI: 10.1039/C6TA08691H.

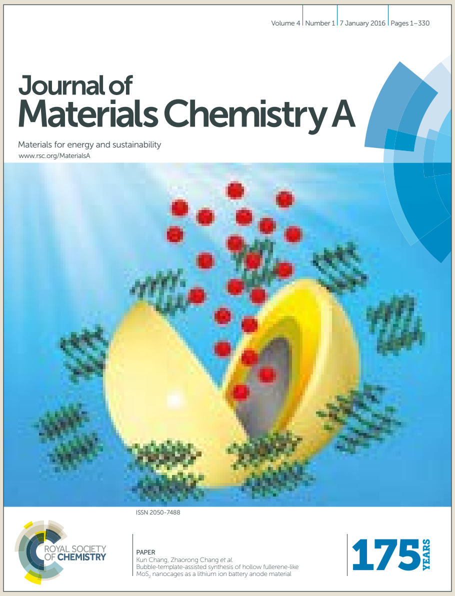

ROYAL SOCIETY
OF CHEMISTRY

rsc.li/materials-a

View Article Online
DOI: 10.1039/C6TA08691H

Journal Name

ARTICLE

Received 00th January 20xx,
Accepted 00th January 20xx

DOI: 10.1039/x0xx00000x

www.rsc.org/

Bio-directed Morphology Engineering Towards Hierarchical 1D to 3D Macro/meso/nanoscopic *Morph*-tunable Carbon Nitride Assemblies for Enhanced Artificial Photosynthesis

Jun Xu,[ab] Han Zhou,*[ab] Kaiyu Shi,[a] Runyu Yan,[a] Yiwen Tang,[a] Jian Liu,[e] Jinhua Ye,[cd] Di Zhang[a] and Tongxiang Fan*[a]

The design of artificial photosynthetic systems (APS) with hierarchical porosity by taking into account of liquid flow and gas transport effects is of high significance. Herein we demonstrate a general and facile strategy to prepare hierarchical 1D to 3D macro/meso/nanoscopic *morph*-tunable g-C_3N_4 assemblies *via* bio-directed morphology engineering for enhanced artificial photosynthesis of CO and methane *via* CO_2 reduction. *Escherichia coli* (1D), *Papilio nephelus* wings (2D, planar) and cole pollen (3D) are adopted for 1D to 3D multiscale assemblies with high surface areas *via* a two-step transformation process. Moreover, liquid flow and gas diffusion behaviors are investigated using COMSOL computational simulation to reveal the relationship between structural effects and output efficiency theoretically. Such methodology can be extended to realize versatile fabrication of various *morph*-tunable carbon nitride assemblies. Importantly, this research illustrates the power of combining theoretical calculations and experimental techniques to achieve the controlled design of high efficiency APS, may provide further avenues to APS optimization.

Introduction

Solar energy conversion by artificial photosynthetic systems (APS) that is inspired by natural leaves is thought to be a potential and promising approach for solving energy crisis.[1-3] The photochemical transformation of CO_2 into hydrocarbon fuels (such as CO, CH_4, HCOOH, and so on) has emerged as a research hotspot.[4-7] However, CO_2 conversion efficiency in artificial photosynthesis is still very low comparing with photocatalytic hydrogen evolution. For the gas involved CO_2 reduction reactions, gas transport in the gas channels and within the porous materials is one limiting factor and tends to affect the activities at some extent. However, there are very few studies on such exploration.[8,9] Hierarchical assemblies featuring the combination of macroscopic and microscopic structures could in principle allow for enhanced liquid flow and gas transport in liquid-phase reaction systems.[10,11] Thus designing of artificial photosynthetic systems with hierarchical porosity is of high significance. Further investigating of liquid flow and gas transport from the theoretical aspects will deepen understandings between the performance and hierarchical morphology.

Graphitic carbon nitride (g-C_3N_4) is a promising material with wide applications in photocatalytic solar energy conversion,[12,13] NADH regeneration,[14] CO_2 activation,[15] ion actuators,[16] chemical sensors,[17] biological imaging,[18] piezoelectricity[19] and so forth.[20-22] To date, various nanoarchitectural g-C_3N_4, including 1D nanorods and nanowires, 2D nanosheets, and 3D architectures, have been developed *via* hard/soft template synthesis,[23-25] solvothermal/molten-salt technology,[26] exfoliation methods[18,27] and supermolecular chemistry.[28] The morphology, electronic structure, optical properties and functions of g-C_3N_4 can be efficiently regulated through nanostructure engineering.[29-32] However, the current approaches are limited to exotemplating (for 0D and 1D materials) and exfoliation (for 2D materials) strategies.[27,33-35] Assembling low-dimensional building blocks into bioinspired hierarchical architectures with superior performance is a promising but challenging task. Jun and Stucky et al. developed a molecular cooperative assembly strategy for the construction of 3D macroscopic assemblies of carbon nitride.[36] Nevertheless, a more general and effective transformation strategy for multiscale *morph*-tunable assemblies will be more appealing.

Nature has a variety of hierarchical morphologies ranging from 1D to 3D structures that generate sophisticated functions, such as light manipulation,[37-39] transportation,[40-42]

---

[a] State Key Lab of Metal Matrix Composites, Shanghai Jiaotong University, Shanghai 200240, China.
*E-mail: hanzhou_81@sjtu.edu.cn; txfan@sjtu.edu.cn.
Fax: +86-21-34202749; Tel: +86-21-54747779.
[b] Advanced Energy Material and Technology Center; Shanghai Jiaotong University, Shanghai 200240, China.
[c] International Center for Materials Nanoarchitectonics (MANA), National Institute for Materials Science (NIMS), 1-1 Namiki, Tsukuba, Ibaraki 305-0044, Japan.
[d] TU-NIMS Joint Research Center, School of Materials Science and Engineering, Tianjin University, 92 Weijin Road, Nankai District, Tianjin 300072, China.
[e] Department of Chemistry, Northwestern University, Evanston, 60208, USA.

† Electronic Supplementary Information (ESI) available: See DOI: 10.1039/x0xx00000x

gas diffusion.[43] Bio-directed morphology engineering would allow facile tailoring of morphology and physical properties.[44,45] However, there are few reports on constructing multiscale carbon nitride architectures by this bio-directed strategy.[46] Herein we demonstrate a general and facile synthetic strategy to prepare hierarchical 1D to 3D macro/meso/nanoscopic *morph*-tunable carbon nitride assemblies *via* bio-directed morphology engineering for enhanced artificial photosynthesis of CO and methane *via* CO_2 reduction. Three typical kinds of biological systems, *Escherichia coli* (1D), *Papilio nephelus* butterfly wings (2D, planar) and cole pollen (3D) are employed in the current study. Two-step transformation process is applied for the construction of 1D to 3D macro/meso/nanoscopic carbon nitride assemblies with high surface areas (Scheme 1). Moreover, liquid flow and gas diffusion behaviors are investigated using COMSOL multiphysics computational simulation to reveal the relationship between structural effects and output efficiency theoretically. To our knowledge, this is the first report of a comprehensive theoretical modelling and understanding for liquid flow and gas diffusion within hierarchical porous materials in artificial photosynthesis. More importantly, this research combining theoretical calculations and experimental techniques in the controlled design of APS, may provide further avenues to APS optimization.

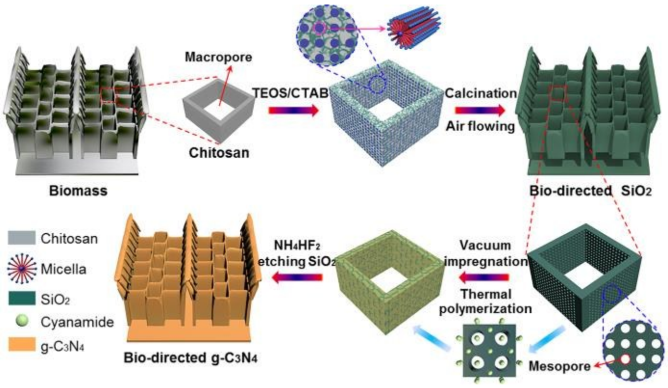

Scheme 1. Schematic illustration for the fabrication of macro/meso/nanoscopic *morph*-tunable g-C_3N_4 with butterfly wing template as an example *via* a two-step transformation process.

Experimental

Materials

Escherichia coli samples were provided by Beijing Beina Chuanglian Biotechnology Institute. *Papilio nephelus* butterfly wings were provided by Shanghai Qiuyu Biological Technology Co., Ltd. Wall-broken cole pollen was provided by Shengzhou Siming Mountain apiculture Co., Ltd. All the commercially available solvents and reagents were used without further purification.

Synthesis of g-C_3N_4

Bio-directed g-C_3N_4 was synthesized *via* a two-step transformation method. Firstly, three bio-templates were pretreated by different methods. *Escherichia coli* was fixed by 2.5% glutaraldehyde solution and dehydrated by ethanol with graded concentrations before slightly drying at 30 °C to obtain a solid sample. Butterfly wings of *Papilio nephelus* were soaked in ethanol for 10 min, followed by immersing in 4 wt% NaOH solution for 2 h, and then they were thoroughly rinsed with deionized water, followed by drying at 60 °C to be used. The wall-broken cole pollen was washed with ethanol under magnetic stirring for three times, once 20 min and then dried at 60 °C. Bio-directed SiO_2 was synthesized through a surface sol-gel process with hexadecyltrimethylammonium bromide (CTAB, ≥ 99.0%) as the surfactant. In a typical procedure, CTAB (6.0 g) was dissolved in pure water (30 mL) with magnetic stirring at 60 °C for 15 min. Secondly, 1.4 M HCl solution (30 mL) was added to ethyl silicate (TEOS, $SiO_2 \geq 28.4\%$, 16 g) dissolved in ethanol (180 mL). The high volume ratio of ethanol -to-H_2O prevented silica from precipitating. Afterwards, the two solutions were mixed together and stirred for another 10 min to obtain a sol. The pretreated *Escherichia coli*, butterfly wings and cole pollen were immersed into the sol for 12 h at room temperature and subsequently pulled out to rinse and dry at 60 °C, followed by calcination under continuous air flowing at 600 °C for 12 h with a heating rate of 1 °C/min to remove the organic constituents, and the residues were bio-directed SiO_2 samples.

In the second step, SiO_2 samples were activated with 1 M HCl solution for 10 min, followed by centrifuging and washing until pH constant at 7. After vacuum drying at 60 °C, the pretreated SiO_2 samples were immersed in cyanamide solution (SiO_2/Cyanamide=1/1, w/w). Afterwards, the suspension was brought into vacuum impregnation at 60 °C for 12 h, and then centrifuged, washed and dried at 60 °C. After that, the obtained white mixture was sintered under continuous Ar flowing at 550 °C for 4 h with a heating rate of 2.3 °C/min to obtain SiO_2/g-C_3N_4 hybrids. Finally, the resultant yellow powder was treated with 4M NH_4HF_2 solution at room temperature for 48 hours to eliminate the silica template, and the precipitate was then centrifuged and thoroughly washed three times with deionized water and ethanol before drying at 80 °C in a vacuum oven overnight. The ultimate products were bio-directed g-C_3N_4 with different architectures.

Bulk g-C_3N_4 was obtained by sintering cyanamide under continuous Ar flowing at 550 °C for 4 h with a heating rate of 2.3 °C/min.

Loading of co-catalysts

The loading of 1 wt% Au on g-C_3N_4 photocatalyst was conducted by a precipitation method using $HAuCl_4$ as the Au source.[47] Typically, g-C_3N_4 (1.95 g) was immersed in 10 mM $HAuCl_4$ solution (10 mL) under vigorous stirring at 70 °C for 4 h, with pH value of 9 adjusted by 0.2 M NaOH solution. The photocatalyst was then recovered, filtered, washed with deionized water, and dried at 100 °C overnight before heat preservation at 200 °C for 4 h in air with a heating rate of 5 °C/min.

View Article Online
DOI: 10.1039/C6TA08691H

The loading of 1 wt% RuO_2 was performed according to an established method reported previously.[8] Firstly, photocatalyst powder (986.8 mg, after loading of 1 wt% Au co-catalysts) was impregnated with the solution of triruthenium dodecacarbonyl ($Ru_3(CO)_{12}$, ≥ 99%, 21.1 mg) in tetrahydrofuran (THF, 20 mL). The mixed samples were continually stirred at 60 °C for 4 h, then dried at 60 °C, and the powder obtained was calcined at 350 °C in air for 2 h to convert ruthenium complex species to ruthenium oxide.

Characterization

The morphologies were characterized with a field emission scanning electron microscopy (SEM, Hitachi S-4800) and transmission electron microscopy (TEM, JEM-2100F). Raw *Escherichia coli* samples were characterized by a biological TEM (Tecnai G2 spirit Biotwin, FEI). The samples were examined by the X-ray diffractometer (XRD, Rigaku, D-max/2550) with Cu Kα radiation (λ=0.154 nm). Fourier transform infrared spectroscopy (FTIR, Thermo Fisher Scientific, Nicolet 6700) was used to analyze the composition and functional groups of the samples. UV–visible (UV–vis) absorption spectroscopy was recorded using a UV-Vis-NIR Spectrophotometer (PerkinElmer, Lambda 950). X-ray photoelectron spectroscopy (XPS, Kratos, AXIS ULTRA DLD) was utilized to analyze the intramolecular electron valence state and the chemical adsorption analyzer (ASAP 2010 M+C) was adopted to evaluate the surface areas and porosity of the samples. Elemental analysis (EA, Elementar, Vario-EL Cube) was conducted to measure the content of C, N and H in the samples.

Photocatalytic CO_2 reduction

Reduction of CO_2 was carried out in a photocatalytic activity evaluation system (Beijing Aulight technology co., LTD) composed of a CEL-PE300E-3A Xe lamp (PerkinElmer, 300 W) and a 300 mL sealed quartz reactor at ambient temperature. A CEL-NP2000 optical power meter (Beijing Aulight technology co., LTD) was used to test the light intensity on the sample. The average irradiance of the full spectrum is about 690 mW cm^{-2}. For the reaction under visible light, an optical cut-off filter (Beijing perfect light technology co., LTD) was applied to restrict the wavelength of incident light to > 400 nm, decreasing light intensity to 330 mW cm^{-2}. To measure the photocatalytic performance, the gaseous reaction products (CO and CH_4) were detected using a gas chromatography (GC-7920, Beijing Aulight technology co., LTD) with a flame ionization detector (FID) and argon as the carrier gas. In a typical experiment process, catalyst powder (100 mg) was dispersed in a solution (50 mL) consisting of water (40 mL) as the solvent and triethanolamine (TEOA, ≥ 78.0%, 10 mL) as the sacrificial agent under continuous magnetic stirring. Prior to irradiation, the reaction system was evacuated and purged with pure CO_2 for three or more cycles to substitute all the residuary air by CO_2. The evolution of CO and CH_4 was measured using a gas chromatography sampling each hour.

Liquid flow and Gas diffusion simulation

Liquid flow and gas diffusion behaviors were investigated by finite element method (FEM) utilizing the COMSOL multiphysics coupling function (software: COMSOL 5.0). Batteries & Fuel Cells module, CAD Import module, CFD (Computational Fluid Dynamics) module and Chemical Reaction Engineering module were used here to carry out the steady state solution. A quasi-2D butterfly wing structural model was developed analytically and the dimension parameters of the simulation system were derived from SEM images. The inverse V-type ridges, disordered columnar pillars and basal substrate were ignored using periodic boundary conditions to simplify the calculation. The non-structural model was established by squeezing the corresponding structural model into a rectangle slab with equal volume. In order to reveal the effects of bio-directed macro/meso/nanoscopic architectures, models for Laminar Flow and Transport of Diluted Species were used to simulate the process of liquid flow, chemical reaction as well as gas diffusion within a periodic repeating unit. Detailed data used in the simulation and calculation could be found in the supporting information.

Results and discussion

Escherichia coli (Figure 1a2), *Papilio nephelus* butterfly wings (Figure 1b2) and wall-broken cole pollen (Figure 1c2) are selected as 1D, 2D and 3D architectures models respectively because of their large variety and species-specific (Figure S1). Here butterfly wing serves as 2D planar prototype because of its film feature though its elaborated structures are more complex than traditional 2D concept. Typically, the biomass was first converted into SiO_2 with CTAB as surfactant to obtain high specific surface area and the bio-directed SiO_2 was subsequently templated into $g\text{-}C_3N_4$ with cyanamide as the precursor followed with the removal of SiO_2 (Scheme 1). SEM images demonstrate the replication of the original morphologies of the biomass into the resulting SiO_2 and $g\text{-}C_3N_4$

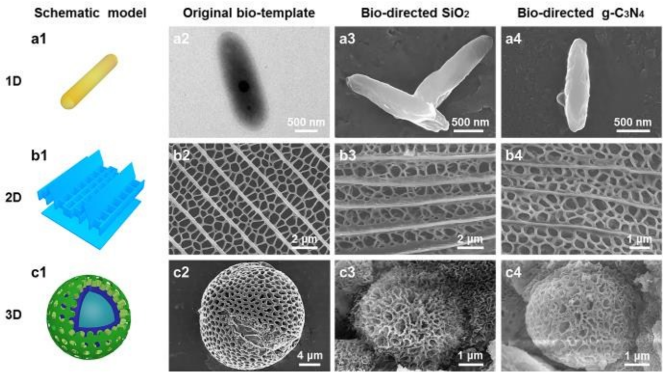

Figure 1. Schematic models, SEM and TEM images of the original biological templates, the bio-directed SiO_2 and $g\text{-}C_3N_4$ samples, respectively. The 1D, 2D and 3D architectures refer to *Escherichia coli* (a1, a2, a3, a4), *Papilio nephelus* butterfly wings (b1, b2, b3, b4) and wall-broken cole pollen (c1, c2, c3, c4), respectively.

View Article Online
DOI: 10.1039/C6TA08691J

(Figure 1). Distinctions mainly lie in the shrinkage of the dimensions caused by the heat treatment process. Hierarchical macro/meso/nanoscopic *morph*-tunable carbon nitride has a number of macropores particularly for 2D and 3D assemblies (Figure 1b4 and 1c4). N_2 adsorption−desorption isotherms further demonstrate their hierarchical porosity. The adsorption−desorption isotherms for bio-directed SiO_2 (Figure 2a) demonstrate the existence of mesopores with wide size distribution. The BET surface area of bio-directed SiO_2 has been remarkably improved (up to 734.63 m^2 g^{-1}) after CTAB was added as a surfactant (Table S1), which is largely derived from the self-assembly of CTAB into micellar structure and incorporating into silica network to create nanopore channels after calcination.[48] By contrast, the surface area of SiO_2 replica without CTAB is only 45 m^2 g^{-1}. The resulting g-C_3N_4 has higher surface area of 71 m^2 g^{-1} (cole pollen-directed g-C_3N_4) and pore volume of 0.16 cm^3 g^{-1} (Table S1).

Both bulk g-C_3N_4 and bio-directed g-C_3N_4 samples possess almost the same X-ray diffraction (XRD) patterns (Figure S2a) with slight diminishment of diffraction peaks of the bio-directed samples. The FTIR spectra of the bio-directed g-C_3N_4 (Figure 2b) exhibit characteristic stretching vibration of aromatic CN heterocycles between 1200 cm^{-1} and 1650 cm^{-1} and breathing vibration of triazine or heptazine units at around 808 cm^{-1}, analogous to those of bulk g-C_3N_4. The product with C/N atomic ratio close to 0.65 (Table S2) could be identified as nitrogen-rich g-C_3N_4.[49,50] Additionally, a trace of hydrogen (~2 wt%) derived from the uncondensed amino functions and adsorbed water was detected through the elemental analysis, which is also verified by FTIR spectrum.[51,52] Three distinct peaks in C 1s spectra at 284.8, 287.5 and 288.3 eV can be identified by XPS spectrum (Figure S2b), corresponding to the graphite carbon species, C−NH_2 species and sp^2-hybridizedcarbon (N−C=N) from the g-C_3N_4, respectively.[53] Figure 2c shows two peaks presented in N 1s spectra. The dominative N 1s peak centered at 398.8 eV is defined as graphite-like sp^2-hybridized nitrogen (C=N−C) in g-C_3N_4. Besides, the other peak at 401.1 eV is regarded as amino functions (C−N−H).[13] From the UV/vis absorption spectra (Figure 2d), the red-shift of absorption edge of butterfly wing-directed g-C_3N_4 was observed. Typical semiconductor absorption with a bandgap of 2.74 eV is observed for butterfly wing-directed g-C_3N_4 while the value of 2.77 eV is determined for bulk g-C_3N_4.

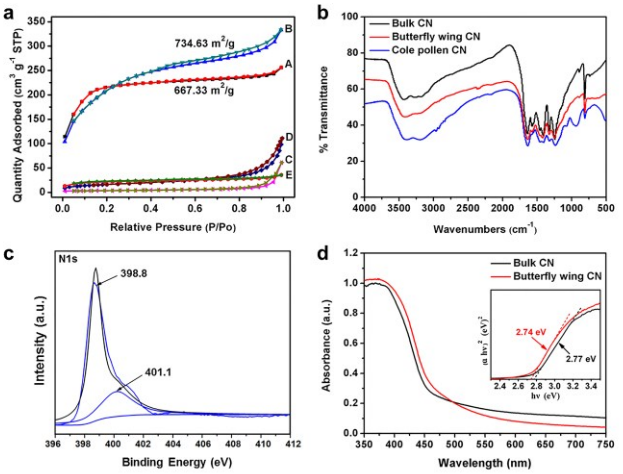

Figure 2. (a) Nitrogen adsorption−desorption isotherms of the SiO_2 and g-C_3N_4 samples. A, B, C, D and E refer to butterfly wing-directed SiO_2, cole pollen-directed SiO_2, bulk g-C_3N_4, butterfly wing-directed g-C_3N_4 and cole pollen-directed g-C_3N_4, respectively. (b) FTIR spectra of the bulk g-C_3N_4 and bio-directed g-C_3N_4. (c) XPS spectra of N 1s for the butterfly wing-directed g-C_3N_4. (d) UV-vis absorption spectra and (inset) plots of $(\alpha hv)^2$ *vs* (hv) for the g-C_3N_4 samples. The dotted lines are the tangents to the curves. The cross value of the X axis is the band gap.

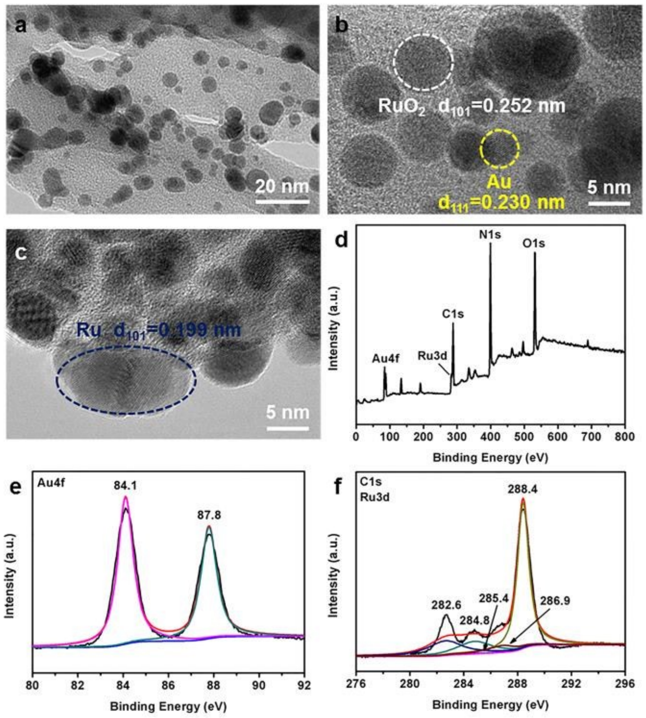

Figure 3. (a) TEM image of the Au and RuO_2 loaded bio-directed g-C_3N_4 samples. (b) And (c) HRTEM micrograph of the Au and RuO_2 loaded bio-directed g-C_3N_4 samples. (d) XPS survey spectra, (e) high-resolution XPS spectra of Au 4f, (f) high-resolution XPS spectra of C 1s and Ru 3d for the Au and RuO_2 loaded bio-directed g-C_3N_4 samples, respectively.

Nanometer-sized Au and RuO_2 with a grain size ranging from 4 to 10 nm were directly deposited on the bare surface of g-C_3N_4, as was observed in extensive TEM studies (Figure 3a). The clear lattice fringe of 0.230 nm can be attributed to the (111) facets of Au.[54,55] Besides, the interplanar spacing of some other crystalline grains was calculated to be 0.252 nm, corresponding to the orientation of atomic plane (101) in the rutile RuO_2 (Figure 3b).[56] However, extremely trace of Ru

View Article Online
DOI: 10.1039/C6TA08691H

metal (d_{101}=0.199 nm) can also be observed (Figure 3c), which could be the by-product of ruthenium oxide reduction.[57] XPS was carried out to examine the presence of Au and RuO_2. C 1s, N 1s, O 1s, Au 4f and Ru 3d peak can be detected obviously (Figure 3d). Au $4f_{7/2}$ and $4f_{5/2}$ binding energies of 84.1 and 87.8 eV respectively, were observed in the XPS spectrum (Figure 3e), which confirms the presence of Au with zero-valent state.[58] Moreover, the Ru 3d peak is very close to C 1s peaks (Figure 3f). The Ru 3d spectrum was fitted with two primary spinorbit components at 282.6 and 285.4 eV for Ru $3d_{5/2}$ and Ru $3d_{3/2}$ respectively, which corresponds to the binding energy of Ru^{4+} and suggests the presence of RuO_2 in the composites.[59]

Artificial photosynthesis is operated on g-C_3N_4 based systems in a liquid-phase reaction using triethanolamine (TEOA) as the sacrificial agent under visible light irradiation (λ > 400 nm). Bare g-C_3N_4 evolved CO and CH_4 as the main products. Other possible products including formic acid, formaldehyde or methanol were not detected, presumably due to the strong oxidizing ability of photoexcited holes (or OH radicals), which are able to react with the intermediates and products.[60-62] The net hydrocarbon production was negligible. As expected, butterfly wing-directed g-C_3N_4 (termed bio-directed CN) without cocatalysts exhibited about 60% improvements in activities comparing with the bulk g-C_3N_4 (termed bulk CN) (Figure 4a).

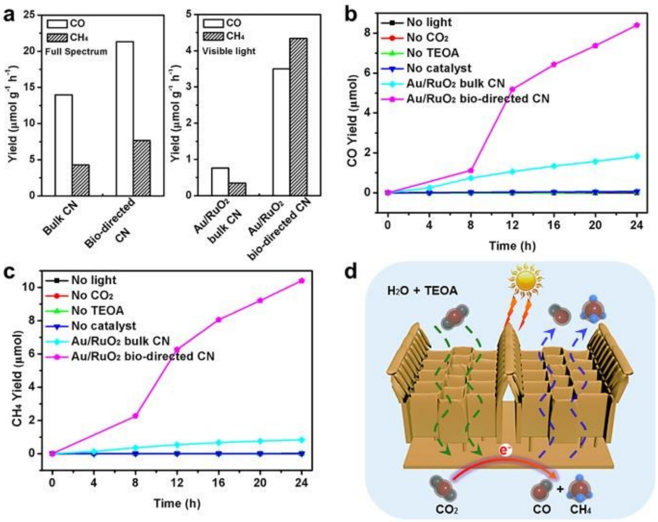

Figure 4. (a) Photocatalytic activity comparisons between bulk g-C_3N_4 and bio-directed g-C_3N_4. (b) And (c) typical time course of photocatalytic CO and CH_4 evolution in liquid-phase system with 20 vol% TEOA as the sacrificial agent under visible light irradiation (λ>400 nm), respectively. (d) Scheme of the artificial photosynthesis processes over butterfly wing-directed g-C_3N_4.

Co-catalysts were loaded to promote the activity. Au functions as an effective cocatalyst to accelerate CO_2 reduction.[63] After loading with 1 wt% Au, Au bio-directed CN evolved approximately 4.09 μmol of CO after 24 h irradiation, which is 4.1 times as much as that of Au bulk CN (Figure S3). In addition, the photocatalytic activity could be further improved after deposition of 1 wt% RuO_2 co-catalyst (Figure 4b and 4c). Ruthenium and its complexes could assist to photocatalyze or electrocatalyze CO_2 reduction to form CO or HCOOH with high selectivity and quantum yields.[64,65] It is worth noting that an obvious promotion nearly 3.6 folds for CO evolution can be observed when compared Au/RuO_2 bio-directed CN with Au/RuO_2 bulk CN. The CH_4 yield reached 4.34 μmol g^{-1} h^{-1} for Au/RuO_2 bio-directed CN, 11.6 times higher than that of Au/RuO_2 bulk CN (Figure 4a and 4c).

Oxygen was not detected in the current study. The oxygen produced by the water splitting is possibly partially consumed by the oxygen vacancies on photocatalyst surface and partially employed for oxidizing the evolved products.[66,67] Control experiments were cautiously performed. Without either of TEOA, photocatalyst or light, almost no CO and CH_4 could be detected. When using Ar gas instead of CO_2, only traces of products were detected because of the photoreduction of residual CO_2 adsorbed on the photocatalyst surfaces. Since there is about 2 ppm of CO and 1 ppm of CH_4 in the atmosphere, CO and CH_4 in the above control experiments are partly regarded as contaminations from the natural air during sampling.[8] These results strongly suggest that g-C_3N_4 undergoes photoexcitation with visible light irradiation, separating the photon-generated electrons and holes. Subsequently, electrons in the conduction band are consumed by CO_2 reduction and holes in the valence band are captured by TEOA. We compared our results with other CO_2 photoreduction systems and the data is listed in Table 1. However, because the experimental conditions (light intensity, wavelength range, irradiation distance, reaction temperature, reaction medium and others) are different, the photocatalytic performances vary considerably.

We attribute the activity improvements in APS to the synergy of high liquid flow and gas diffusion efficiency due to the multiscale macro/meso/nanoscopic architectures, and more reactive sites originating from high specific surface areas (Figure 4d). The surface area factor is a well-known one and widely investigated already.[68-72] Whereas the CO_2 photoreduction was conducted in a liquid-phase system involving processes of liquid flow and gas diffusion which are important factors for the catalytic reactions, so here we focus on liquid flow and gas diffusion behaviors using COMSOL computational simulation method to reveal the relationship between structural effects and output efficiency theoretically. Finite element method (FEM) based on two major physical models (Laminar Flow and Transport of Diluted Species)[73,74] was conducted for the simulation within a macro/meso/nanoscopic periodic repeating unit based on a quasi-2D butterfly wing-directed model (Figure 5a1). After loading with Au and RuO_2 co-catalysts respectively, the g-C_3N_4 assemblies still retain the original hierarchical morphologies as revealed by SEM and EDS mapping (Figure S4). Thus the simulation based on such bio-directed structures is reasonable and convincing. The inverse V-type ridges, disordered columnar pillars and basal substrate were all simplified using

View Article Online
DOI: 10.1039/C6TA08691H

Table 1. Comparison with other CO_2 photoreduction systems to form CO and hydrocarbons.

Light source	Catalyst	Co-catalyst	Reaction medium	Main product (μmol g^{-1} h^{-1})	Ref.
Nonfocus 300 W Xe lamp, visible light (λ> 420 nm)	Helical nanorod-like g-C_3N_4	0.43 wt% $CoCl_2$	Bipyridine (15 mg), H_2O (1 mL), acetonitrile (3 mL), triethanolamine (1 mL)	CO (296.7)	82
500 W Xe lamp, visible light (λ> 420 nm)	g-C_3N_4	6 wt% ZnO	Deionized water (4 mL) vapor	CO (29.5)	83
300 W high pressure Xe lamp	Mesoporous phosphorylated g-C_3N_4	—	4 M H_2SO_4 (5 mL), $NaHCO_3$ (1.0 g)	CH_4 (78.0)	84
300 W Xe arc lamp	Amine-functionalized g-C_3N_4	—	2 M H_2SO_4 (0.3 mL), $NaHCO_3$ (0.084 g)	CH_4 (0.34)	85
300 W Xe arc lamp	g-C_3N_4	1 wt% Pt	4 M HCl (0.25 mL), $NaHCO_3$ (0.12 g)	CH_4 (0.3)	86
300 W Xe arc lamp	g-C_3N_4 nanosheets	1 wt% Au, 1 wt% ZIF-9	Deionized water (2 mL) vapor	CO (0.5)	87
300 W high pressure Xe lamp, 380 nm monochromatic ligh	g-C_3N_4/BiOBr	Au	4 M H_2SO_4 (5 mL), $NaHCO_3$ (1.3 g)	CO (6.67)	54
300 W Xe arc lamp, visible light (λ> 420 nm)	Leaf-architectured $SrTiO_3$	1 wt% Au	Distilled water (2 mL) vapor	CO (0.35)	8
100 W Xe lamp, UV-vis (λ=320-780 nm)	TiO_2	0.5 wt% Au	Water (4 mL) vapor	CH_4 (3.1)	88
Newport Instruments AM 1.5 solar simulator	TiO_2 nanotube arrays	0.25 μmol Au per wafer	Water droplets (5 μL, 1 mm diameter)	CH_4 (58.47)	55
400 W high pressure Hg lamp, visible light (λ> 400 nm)	Mesoporous g-C_3N_4	**Ru** complex 3.9 μmol g^{-1}	Acetonitrile and triethanolamine (4 mL ,4 : 1 v/v)	HCOOH (46.35)	89
400 W high pressure Hg lamp, visible light (λ> 400 nm)	g-C_3N_4	**Ru** complex 7.8 μmol g^{-1}	N,N-dimethylacetamide and triethanolamine (4 mL, 4:1 v/v)	HCOOH (1100)	90
300 W Xe lamp, visible light (λ> 420 nm)	Bio-directed hierarchical porous g-C_3N_4	1 wt% Au, 1 wt% RuO_2	Water and triethanolamine (4:1 v/v)	CH_4 (4.34)	This work

periodic boundary conditions (Figure 5a1) with dimension parameters shown in Figure S5a. The non-structural model for comparison was established by squeezing the corresponding structural model into a rectangle slab with equal volume (Figure 5a2).

The liquid flow in the structures is modeled with the Laminar Flow interface that solves the Navier-Stokes equations at steady state[73] (Basic data for the simulation listed in Table S3). The numerical modules with long entrance established by software (Figure 5b1 and 5b2) designate the flow direction of external liquid with periodic boundary condition. The aqueous solution can circulate in the hierarchical macro/meso/nanoscopic holes and reacts on the surfaces of the whole substrate (Figure 5c1). Contrastively, only the external surface is exposed to be contacted in the non-structural model (Figure 5c2). The substance concentration and velocity field within the internal structures would change accordingly as time goes on, until the realization of steady state. Figure 5e1 and 5e2 demonstrate that the flow velocity of the liquid in the bio-directed model with hierarchical architectures gains more than 60% improvements as compared to the non-structural model. Additionally, vortexes are formed around the hole wall of the porous structure (Figure 5f1 and 5f2), which partly facilitate the sufficient contact and mass transport of the reacting species, thus speeding up the reaction kinetically.[75,76]

The catalytic reaction occurred in the APS was assumed to be a surface reaction (Figure S5b and S5c). The mass balances were set up with the Transport of Diluted Species interface and solves the diffusion-convection equations at steady state.[74] Gas diffusion behavior is discussed to have a better understanding of structural effects on catalytic efficiency. Differences of gas diffusion mechanism in micro-nano-scale distinguish the two models.[77] Gas diffusion in the bio-directed model with hierarchical pores on a scale ranging from nanometer to submicrometre is determined by synergistic effect of molecular diffusion, Knudsen diffusion and adsorption layer surface diffusion (Figure 5d1).[74,78] Knudsen diffusion is predominant in mesopores while molecular diffusion occupies a leading position in macropores.[78,79] While for the non-structural model, the molecular diffusion can be ignored and surface diffusion is foremost leaving internal parts not contacting (Figure 5d2) since there is only traces of mesopores existed.[78] The diffusivity of CO_2 and CO (taking as examples) in hierarchical macro/meso/nanoscopic gas channels has been calculated (Supporting information for details). Obviously, the molecular diffusivity in macropores is about 2~4 folds larger than the Knudsen diffusivity in mesopores, both of which are 4 orders of magnitude higher than the surface diffusivity (Table S5). Thus the diffusion efficiency in bio-directed model with hierarchical architectures is definitely superior to the non-structural model.

View Article Online
DOI: 10.1039/C6TA08691H

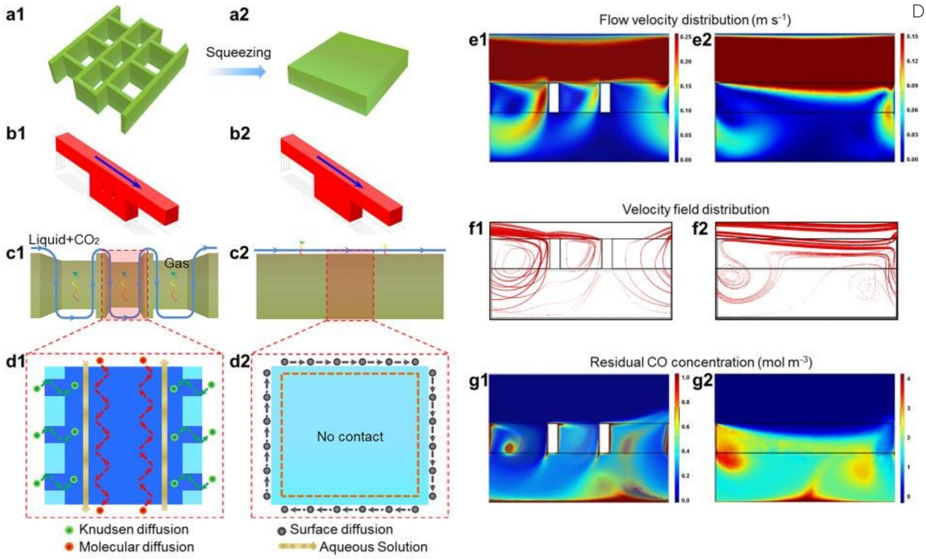

Figure 5. Schematic diagram of the simplified butterfly wing-directed model (a1) and non-structural model (a2) using in the finite element simulation. Numerical modules of the bio-directed model (b1) and non-structural model (b2) with periodic boundary condition. The blue arrow represents the direction of fluid flow. Sketch of fluid flow and the major gas diffusion mechanism for the bio-directed model (c1, d1) and non-structural model (c2, d2), respectively. The simulation results of flow velocity distribution, velocity field distribution and residual CO concentration on the bio-directed model (e1, f1, g1) and non-structural model (e2, f2, g2) surface, respectively.

Based on the higher gas diffusion efficiency, the reactants (CO_2) can diffuse much faster within the bio-directed hierarchical framework. Meanwhile, the higher surface areas and more mesopores increase the local CO_2 concentration which can prolong the hold-up time of CO_2 in gas channels.[11,80] Thus we can infer that the reaction rate is faster because of the aggregation of CO_2 in the hierarchical porous framework.[81] During the reaction, the main products CO and CH_4 are released into the medium. The diffusion of released gases (taking CO as an example) was simulated based on the Equation S4 and S5 in the supporting information. Astonishingly, the average CO concentration (integral from Figure 5g1 and 5g2) residual in the bio-directed model (0.45 mol m^{-3}) is about a quarter of that in the non-structural model (1.9 mol m^{-3}) (Supporting information for details) in spite of a faster reaction rate, which means more CO has been released. So it is reasonable to conclude that the diffusion of reaction products has been greatly facilitated in the bio-directed structures.

Above all, the macroscopic output efficiency has been significantly improved, closely relevant to the structure effects. First, the multiscale macro/meso/nanoscopic architectures facilitate the liquid flow. Second, gas transport is promoted by the mutual effect of hierarchical macro/mesoporous, including CO_2 entrance to the reactive sites and products release to external liquid medium effectively. Last but not the least, high porosity and surface areas contribute to increase the local CO_2 concentration. The simulation results support the experiments well and give a deep understanding of the processes.

Conclusions

In summary, we have proposed a general approach for the fabrication of hierarchical 1D to 3D macro/meso/nanoscopic *morph*-tunable carbon nitride assemblies *via* bio-directed morphology engineering. We believe that such approach can be extended to a large variety of biomass with hierarchical architectures for realizing versatile fabrication of *morph*-tunable functional assemblies (not limited to carbon nitride). The CO_2 photoreduction activity improvements are attributed to the synergy of high liquid flow and gas diffusion efficiency arising from the multiscale macro/meso/nanoscopic architectures, and more reactive sites derived from high specific surface areas. We anticipate that suitable structure modulations might be applied on other APS to meet the optimal mass transport requirements. Moreover, this strategy provides the insight for designing a new family of APS by tuning morphology and functionality, and may also shed light on fundamental mechanisms of artificial photosynthesis processes.

Acknowledgements

We are grateful for financial support by the Foundation for National Natural Science Foundation of China (51425203), the Author of National Excellent Doctoral Dissertation of PR China (201434), Innovation Program of Shanghai Municipal Education Commission (15ZZ008), Program of Shanghai

Subject Chief Scientist (15XD1501900), Shanghai Rising-Star Program (15QA1402700) and International Science & Technology Cooperation Program of China (2015DFE52870).

Notes and references

1 J. Marshall, *Nature*, 2014, **510**, 22-24.
2 M. D. Karkas, O. Verho, E. V. Johnston and B. Akermark, *Chem. Rev.*, 2014, **114**, 11863-12001.
3 M. Rudolf, S. V. Kirner and D. M. Guldi, *Chem. Soc. Rev.*, 2016, **45**, 612-630.
4 Q. Kang, T. Wang, P. Li, L. Liu, K. Chang, M. Li and J. Ye, *Angew. Chem. Int. Ed. Engl.*, 2015, **54**, 841-845.
5 K. K. Sakimoto, A. B. Wong and P. Yang, *Science*, 2016, **351**, 74-77.
6 H. Zhou, R. Yan, D. Zhang and T. Fan, *Chem. Eur. J.*, 2016, **22**, 9870-9885.
7 W. H. Wang, Y. Himeda, J. T. Muckerman, G. F. Manbeck and E. Fujita, *Chem. Rev.*, 2015, **115**, 12936-12973.
8 H. Zhou, J. Guo, P. Li, T. Fan, D. Zhang and J. Ye, *Sci. Rep.*, 2013, **3**, 1667.
9 H. Zhou, P. Li, J. Guo, R. Yan, T. Fan, D. Zhang and J. Ye, *Nanoscale*, 2015, **7**, 113-120.
10 S. Dutta, A. Bhaumik and K. C. W. Wu, *Energy Environ. Sci.*, 2014, **7**, 3574-3592.
11 D. Schneider, D. Mehlhorn, P. Zeigermann, J. Karger and R. Valiullin, *Chem. Soc. Rev.*, 2016, **45**, 3439-3467.
12 X. Wang, K. Maeda, A. Thomas, K. Takanabe, G. Xin, J. M. Carlsson, K. Domen and M. Antonietti, *Nat. Mater.*, 2009, **8**, 76-80.
13 J. Liu, Y. Liu, N. Liu, Y. Han, X. Zhang, H. Huang, Y. Lifshitz, S.-T. Lee, J. Zhong and Z. Kang, *Science*, 2015, **347**, 970-974.
14 J. Liu and M. Antonietti, *Energy Environ. Sci.*, 2013, **6**, 1486.
15 F. Goettmann, A. Thomas and M. Antonietti, *Angew. Chem. Int. Ed. Engl.*, 2007, **46**, 2717-2720.
16 G. Wu, Y. Hu, Y. Liu, J. Zhao, X. Chen, V. Whoehling, C. Plesse, G. T. Nguyen, F. Vidal and W. Chen, *Nat. Commun.*, 2015, **6**, 7258.
17 E. Z. Lee, Y. S. Jun, W. H. Hong, A. Thomas and M. M. Jin, *Angew. Chem. Int. Ed. Engl.*, 2010, **49**, 9706-9710.
18 X. Zhang, X. Xie, H. Wang, J. Zhang, B. Pan and Y. Xie, *J. Am. Chem. Soc.*, 2013, **135**, 18-21.
19 M. Zelisko, Y. Hanlumyuang, S. Yang, Y. Liu, C. Lei, J. Li, P. M. Ajayan and P. Sharma, *Nat. Commun.*, 2014, **5**, 4284.
20 Y. Zheng, L. Lin, B. Wang and X. Wang, *Angew. Chem. Int. Ed.*, 2015, **54**, 12868-12884.
21 J. Liu, H. Wang and M. Antonietti, *Chem. Soc. Rev.*, 2016, **45**, 2308-2326.
22 W. J. Ong, L. L. Tan, Y. H. Ng, S. T. Yong and S. P. Chai, *Chem. Rev.*, 2016, **116**, 7159-7329.
23 J. Liu, J. Huang, H. Zhou and M. Antonietti, *ACS Appl. Mater. Interfaces*, 2014, **6**, 8434-8440.
24 J. Liu, H. Wang, Z. P. Chen, H. Moehwald, S. Fiechter, R. van de Krol, L. Wen, L. Jiang and M. Antonietti, *Adv. Mater.*, 2015, **27**, 712-718.
25 J. Wang, C. Zhang, Y. Shen, Z. Zhou, J. Yu, Y. Li, W. Wei, S. Liu and Y. Zhang, *J. Mater. Chem. A*, 2015, **3**, 5126-5131.
26 H. Gao, S. Yan, J. Wang, Y. A. Huang, P. Wang, Z. Li and Z. Zou, *Phys. Chem. Chem. Phys.*, 2013, **15**, 18077-18084.
27 P. Niu, L. Zhang, G. Liu and H.-M. Cheng, *Adv. Funct. Mater.*, 2012, **22**, 4763-4770.
28 M. Shalom, S. Inal, C. Fettkenhauer, D. Neher and M. Antonietti, *J. Am. Chem. Soc.*, 2013, **135**, 7118-7121.
29 J. Zhao, M. A. Holmes and F. E. Osterloh, *Acs Nano*, 2013, **7**, 4316-4325.
30 H. Tong, S. Ouyang, Y. Bi, N. Umezawa, M. Oshikiri and J. Ye, *Adv. Mater.*, 2012, **24**, 229-251.
31 F. E. Osterloh, *Chem. Soc. Rev.*, 2013, **42**, 2294-2320.
32 Y. Zhang, Z. Zhou, Y. Shen, Q. Zhou, J. Wang, A. Liu, S. Liu and Y. Zhang, *ACS Nano*, 2016, **10**, 9036-9043.
33 Y. Chen, C. Tan, H. Zhang and L. Wang, *Chem. Soc. Rev.*, 2015, **44**, 2681-2701.
34 J. Zhang, Y. Chen and X. Wang, *Energy Environ. Sci.*, 2015, **8**, 3092-3108.
35 B. Luo, G. Liu and L. Wang, *Nanoscale*, 2016, **8**, 6904-6920.
36 Y.-S. Jun, J. Park, S. U. Lee, A. Thomas, W. H. Hong and G. D. Stucky, *Angew. Chem.*, 2013, **125**, 11289-11293.
37 K. H. Jeong, J. Kim and L. P. Lee, *Science*, 2006, **312**, 557-561.
38 J. J. Kim, Y. Lee, H. G. Kim, K. J. Choi, H. S. Kweon, S. Park and K. H. Jeong, *Proc. Natl. Acad. Sci.*, 2012, **109**, 18674-18678.
39 K. Yu, T. Fan, S. Lou and D. Zhang, *Prog. Mater Sci.*, 2013, **58**, 825-873.
40 Y. X. Pan, H. P. Cong, Y. L. Men, S. Xin, Z. Q. Sun, C. J. Liu and S. H. Yu, *Acs Nano*, 2015, **9**, 11258-11265.
41 K. C. Park, P. Kim, A. Grinthal, N. He, D. Fox, J. C. Weaver and J. Aizenberg, *Nature*, 2016, **531**, 78-82.
42 Q. Liu, L. Wen, K. Xiao, H. Lu, Z. Zhang, G. Xie, X. Y. Kong, Z. Bo and L. Jiang, *Adv. Mater.*, 2016, **28**, 3181-3186.
43 P. J. Franks and D. J. Beerling, *Proc. Natl. Acad. Sci.*, 2009, **106**, 10343-10347.
44 H. Zhou, T. Fan and D. Zhang, *ChemSusChem*, 2011, **4**, 1344-1387.
45 S. Wang, K. Liu, X. Yao and L. Jiang, *Chem. Rev.*, 2015, **115**, 8230-8293.
46 J. Liu, R. Cazelles, Z. P. Chen, H. Zhou, A. Galarneau and M. Antonietti, *Phys. Chem. Chem. Phys.*, 2014, **16**, 14699-14705.
47 C. u. Gomes Silva, R. Juárez, T. Marino, R. Molinari and H. García, *J. Am. Chem. Soc.*, 2010, **133**, 595-602.
48 Y. Shin, J. Liu, J. H. Chang, Z. Nie and G. J. Exarhos, *Adv. Mater.*, 2001, **13**, 728-732.
49 A. Thomas, A. Fischer, F. Goettmann, M. Antonietti, J.-O. Müller, R. Schlögl and J. M. Carlsson, *J. Mater. Chem.*, 2008, **18**, 4893.
50 Y. Wang, X. Wang and M. Antonietti, *Angew. Chem. Int. Ed.*, 2012, **51**, 68-89.
51 X. Wang, X. Chen, A. Thomas, X. Fu and M. Antonietti, *Adv. Mater.*, 2009, **21**, 1609-1612.
52 P. Wu, J. Wang, J. Zhao, L. Guo and F. E. Osterloh, *J. Mater. Chem. A*, 2014, **2**, 20338-20344.
53 F. He, G. Chen, Y. Yu, S. Hao, Y. Zhou and Y. Zheng, *ACS Appl. Mater. Interfaces*, 2014, **6**, 7171-7179.
54 Y. Bai, T. Chen, P. Wang, L. Wang, L. Ye, X. Shi and W. Bai, *Sol. Energy Mater. Sol. Cells*, 2016, **157**, 406-414.
55 P. Kar, S. Farsinezhad, N. Mahdi, Y. Zhang, U. Obuekwe, H. Sharma, J. Shen, N. Semagina and K. Shankar, *Nano Res.*, 2016, **9**, 3478-3493.
56 C. C. Hu, K. H. Chang, M. C. Lin and Y. T. Wu, *Nano Lett.*, 2006, **6**, 2690-2695.
57 Y. Lee, J. Suntivich, K. J. May, E. E. Perry and Y. Shao-Horn, *J. Phys. Chem. Lett.*, 2012, **3**, 399-404.
58 K. Nishio and H. Masuda, *Angew. Chem. Int. Ed.*, 2011, **50**, 1603-1607.
59 Z.-S. Wu, D.-W. Wang, W. Ren, J. Zhao, G. Zhou, F. Li and H.-M. Cheng, *Adv. Funct. Mater.*, 2010, **20**, 3595-3602.
60 B. Kumar, M. Llorente, J. Froehlich, T. Dang, A. Sathrum and C. P. Kubiak, *Annu. Rev. Phys. Chem.*, 2012, **63**, 541-569.
61 A. A. Peterson, F. Abildpedersen, F. Studt, J. Rossmeisl and J. K. Nørskov, *Energy Environ. Sci.*, 2010, **3**, 1311-1315.
62 G. Halasi, G. Schubert and F. Solymosi, *J. Phys. Chem. C*, 2012, **116**, 15396-15405.
63 Y. Chen, C. W. Li and M. W. Kanan, *J. Am. Chem. Soc.*, 2012, **134**, 19969-19972.
64 Y. Tamaki, T. Morimoto, K. Koike and O. Ishitani, *Proc. Natl. Acad. Sci.*, 2012, **109**, 15673-15678.
65 J. Wang, J. Zhao and F. E. Osterloh, *Energy Environ. Sci.*, 2015, **8**, 2970-2976.
66 Z. Goren, I. Willner, A. J. Nelson and A. J. Frank, *J. Phys. Chem.*, 1990, **94**, 3784-3790.
67 E. Lira, S. Wendt, P. Huo, J. O. Hansen, R. Streber, S. Porsgaard, Y.

View Article Online
DOI: 10.1039/C6TA08691H

Wei, R. Bechstein, E. Laegsgaard and F. Besenbacher, *J. Am. Chem. Soc.*, 2011, **133**, 6529-6532.

68 T. Wang, X. Meng, P. Li, S. Ouyang, K. Chang, G. Liu, Z. Mei and J. Ye, *Nano Energy*, 2014, **9**, 50-60.

69 L. Shi, T. Wang, H. Zhang, K. Chang and J. Ye, *Adv. Funct. Mater.*, 2015, **25**, 5360-5367.

70 L. Shang, H. Yu, X. Huang, T. Bian, R. Shi, Y. Zhao, G. I. Waterhouse, L. Z. Wu, C. H. Tung and T. Zhang, *Adv. Mater.*, 2016, **28**, 1668-1674.

71 Y. Ma, Y. Jia, L. Wang, M. Yang, Y. Bi and Y. Qi, *Chemistry*, 2016, **22**, 5844-5848.

72 Y. Ma, Y. Jia, Z. Jiao, M. Yang, Y. Qi and Y. Bi, *Chem Commun (Camb)*, 2015, **51**, 6655-6658.

73 M. Fadaei and R. Mohammadi, *Energy Convers. Manage.*, 2015, **106**, 93-100.

74 W. Wang, J. Yao, H. Sun and W.-H. Song, *Pet. Sci.* , 2015, **12**, 664-673.

75 E. L. Cussler, *Diffusion: mass transfer in fluid systems*, Cambridge university press, 2009.

76 D. Martinand and J. C. Vassilicos, *Phys. Rev. E Stat Nonlin Soft Matter Phys.*, 2007, **75**, 036315.

77 W. Kast and C.-R. Hohenthanner, *Int. J. Heat Mass Transfer*, 2000, **43**, 807-823.

78 P. Chinda, S. Chanchaona, P. Brault and W. Wechsatol, *J. Sus. Energy Environ.*, 2010, **1**, 185-196.

79 H. Sun, J. Yao, D.-y. Fan, C.-c. Wang and Z.-x. Sun, *Int. J. Heat Mass Transfer*, 2015, **83**, 192-199.

80 S. Choi, J. H. Drese and C. W. Jones, *ChemSusChem*, 2009, **2**, 796–854.

81 S. Ackermann, L. Sauvin, R. Castiglioni, J. L. Rupp, J. R. Scheffe and A. Steinfeld, *J. Phys. Chem. C*, 2015, **119**, 16452-16461.

82 Y. Zheng, L. Lin, X. Ye, F. Guo and X. Wang, *Angew. Chem. Int. Ed. Engl.*, 2014, **53**, 11926-11930.

83 Y. He, Y. Wang, L. Zhang, B. Teng and M. Fan, *Applied Catalysis B: Environmental*, 2015, **168-169**, 1-8.

84 L. Ye, D. Wu, K. H. Chu, B. Wang, H. Xie, H. Y. Yip and P. K. Wong, *Chem. Eng. J.*, 2016, **304**, 376-383.

85 Q. Huang, J. Yu, S. Cao, C. Cui and B. Cheng, *Appl. Surf. Sci.*, 2015, **358**, 350-355.

86 J. Yu, K. Wang, W. Xiao and B. Cheng, *Phys. Chem. Chem. Phys.*, 2014, **16**, 11492-11501.

87 H. Zhou, P. Li, J. Liu, Z. Chen, L. Liu, D. Dontsova, R. Yan, T. Fan, D. Zhang and J. Ye, *Nano Energy*, 2016, **25**, 128-135.

88 S. Xie, Y. Wang, Q. Zhang, W. Deng and Y. Wang, *ACS Catalysis*, 2014, **4**, 3644-3653.

89 K. Maeda, R. Kuriki, M. Zhang, X. Wang and O. Ishitani, *J. Mater. Chem. A*, 2014, **2**, 15146-15151.

90 R. Kuriki, K. Sekizawa, O. Ishitani and K. Maeda, *Angew. Chem. Int. Ed. Engl.*, 2015, **54**, 2406-2409.

View Article Online
DOI: 10.1039/C6TA08691H

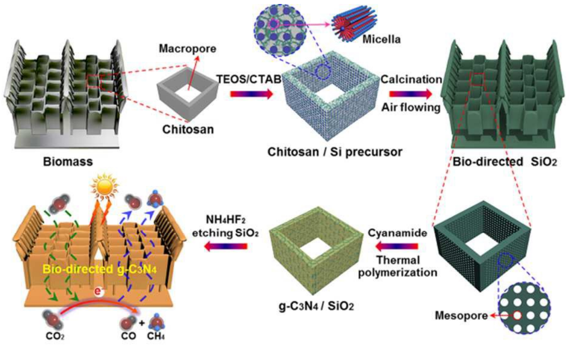

Hierarchical 1D to 3D multiscale *morph*-tunable g-C_3N_4 assemblies were synthesized *via* two-step transformation strategy for enhanced CO_2 photoreduction.